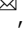## ARTICLE

Check for updates

Field effect control of translocation dynamics in surround-gate nanopores

Makusu Tsutsui [1,6 ✉], Sou Ryuzaki[2,3,6], Kazumichi Yokota [4], Yuhui He[5], Takashi Washio[1], Kaoru Tamada [2] & Tomoji Kawai[1 ✉]

Controlling the fast electrophoresis of nano-objects in solid-state nanopores is a critical issue for achieving electrical analysis of single-particles by ionic current. In particular, it is crucial to slow-down the translocation dynamics of nanoparticles. We herein report that a focused electric field and associated water flow in a surround-gate nanopore can be used to trap and manipulate a nanoscale object. We fine-control the electroosmosis-induced water flow by modulating the wall surface potential via gate voltage. We find that a nanoparticle can be captured in the vicinity of the conduit by balancing the counteracting electrophoretic and hydrodynamic drag forces. By creating a subtle force imbalance, in addition, we also demonstrate a gate-controllable motion of single-particles moving at an extremely slow speed of several tens of nanometers per second. The present method may be useful in single-molecule detection by solid-state nanopores and nanochannels.

[1] The Institute of Scientific and Industrial Research, Osaka University, Ibaraki, Osaka, Japan. [2] Institute of Materials Chemistry and Engineering, Kyushu University, Nishi-ku, Fukuoka, Japan. [3] PRESTO, Japan Science and Technology Agency (JST), Saitama, Japan. [4] National Institute of Advanced Industrial Science and Technology, Takamatsu, Kagawa, Japan. [5] Huazhong University of Science and Technology, Wuhan, China. [6] These authors contributed equally: Makusu Tsutsui, Sou Ryuzaki. ✉email: tsutsui@sanken.osaka-u.ac.jp; kawai@sanken.osaka-u.ac.jp

Solid-state nanopore is a sensor capable of analyzing individual particles and molecules of various sizes[1–3] such as viruses[4,5], extracellular vehicles[6,7], proteins[8–10], and genomes[11–13] dispersed in electrolyte solution. It probes temporal blockage of the ion flow through a hole sculpted in a thin dielectric membrane upon a substance passing through there by electrophoresis[14]. While proven to possess great potential as a versatile nanosensor, the excessively fast and stochastic nature of the translocation dynamics remains to be the central challenge that generally poses critically short residence time along with spatially random positions of analytes in the sensing zone for implementing the electrical analysis[8,15–17]. For instance, whereas biological nanochannels were able to achieve ultraslow DNA translocation speed of about 1 nucleotide per ms by employing a polymerase reaction-derived ratcheting mechanism[18,19], the motion is generally orders of magnitude faster in solid-state nanopores[15] imposing difficulties for single-nucleotide discriminations. Electrophoresis of single-molecule proteins in a nanopore was also reported to be too rapid for detecting the associated ionic blockade current under the given temporal resolution of the ionic current measurements[8]. Meanwhile, despite the significant efforts devoted in the past to add external probes for handling the capture-to-translocation kinetics of single-particles and -molecules, such as optoelectronic[20] and dielectrophoretic approaches[21–23], their abilities are still insufficient to slow-down the nanoscopic objects for the goal of single-protein analyses[10] and nanopore sequencing[15].

Here, aiming to realize an active control of electrophoretically-driven mass transport inside a nanopore, therefore, we employed a field-effect transistor approach[24,25] to regulate the single-nanoparticle translocation dynamics, where we found its capability for holding an object in confined nanospace and manipulating the motions at a 10 nm s^{-1} level by tailoring the interplay between the electrostatic and hydrodynamic forces via a gate control.

Results

Ion transport in surround-gate nanopores. Our device is a gating nanopore comprised of a lithographically-defined 300 nm-sized hole sculpted in a SiN$_x$ membrane of thickness 50 nm with an embedded Pt nano-ring and 20 nm-thick SiO$_2$ gate dielectrics (Fig. 1a–d, see also Supplementary Figs. S1 and S2). The top surface was covered with 5 μm-thick polyimide layer except a 50 μm region around the nanopore to ensure better temporal response[26] of the ionic current as well as to reduce the capacitance-derived noise[27,28]. The cross-membrane ionic current I_{ion} versus voltage V_b characteristics measured in phosphate buffer saline (PBS) showed ohmic behavior with the open conductance G_{open} of 427 nS (Fig. 1e) in agreement to the analytical expression of R_{open} ($=G_{open}^{-1}$) $= R_{pore} + R_{acc} = 2.3$ MΩ within 2% error where $R_{pore} = 4\rho L_{pore}/\pi d_{pore}^2$ and $R_{acc} = \rho/d_{pore}$ are the resistance inside and outside the pore[29,30], respectively, for the channel geometry characterized by the depth $L_{pore} = 90$ nm and the diameter $d_{pore} = 300$ nm with the resistivity $\rho = 0.5$ Ωm of the electrolyte buffer used. Meanwhile, application of the gate voltage V_G in a range from -1 to 1 V to the Pt electrode caused a slight change in the I_{ion}-V_b characteristics manifesting non-negligible influence of the transverse electrostatics on the longitudinal ion transport[31,32].

Single-nanoparticle detections by ionic current measurements. Resistive pulses were observed under positive V_b when one side of the chambers was filled with PBS containing 200 nm-sized carboxylated polystyrene nanoparticles at concentration of 1 pM (Fig. 1f, see also Supplementary Fig. S3). As the I_{ion} traces were featureless under negative voltage, the characteristic signals are naturally ascribed to transient ion blockage by electrophoretically-driven translocation of the negatively-charged polymeric nanobeads (Fig. 1g). Here, the width t_d of the resistive pulses reflects the time single nanoparticles spent to pass through the nanopore, which was as short as 127 μs in case of Fig. 1g under $V_b = 0.5$ V and $V_G = +0.2$ V.

Gate voltage-controlled single-nanoparticle translocation speeds. Single-nanoparticle motion control via transverse electric field is examined by evaluating V_G dependence of t_d. More than a hundred of resistive pulses were recorded at each gate voltage condition from -1.2 to $+1.2$ V at 0.2 V step while keeping V_b at 0.5 V. The pulse widths revealed unimodal distributions (Fig. 2a) except at elevated V_G wherein significantly wider signals were sporadically observed with the longest one being 2.01 s under $V_G = -1.05$ V. In order to see the gating effect more clearly, we exhibited Gaussian fitting and plotted the peak values t_p as a function of the gate voltage (Fig. 2b). The diagram displayed three distinct regimes in terms of the transverse field effect: almost constant t_p at -0.6 V $\leq V_G \leq +0.8$ V (regime I); rise in the translocation time at larger $|V_G|$ for both the positive (regime II) and negative polarities (regime III). The overall tendency was found to be similar when we extended the experiment to 100 nm-sized nanoparticles (Supplementary Fig. S4) except the absence of the prolonged translocation time at $V_G \geq +1.0$ V (Supplementary Fig. S5).

The V_G-derived single-particle dynamics can be interpreted as a consequence of varying contributions of hydrodynamic dragging and columbic interactions under the gate-modulated surface potential at the nanopore wall (Fig. 3a–d)[33–37]. When $V_G < 0$, the negatively-charged nanoparticles are repelled from the wall via the columbic forces[37]. In the meantime, V_b-excited migration of mobile counter cations generates water flow in the direction opposite to the electrophoresis of the polymeric beads (Fig. 3b)[34,35]. Thus, under large negative V_G, the hydrodynamic drag would become comparable to the electrophoretic counterpart, thereby enabling long-term trap of the nanobeads in the nanopore for longer than 0.1 s. At the other extreme, the positive wall surface temporarily adsorbs particles by the attractive coulomb forces (Fig. 3d), which is seen as long plateaus at a certain I_{ion} level (It is worth noting that only a scarce number of nanoparticles were actually immobilized under the positive gate voltages. This reflects the spatially-confined transverse electric field in the nanopore by ion screening (Debye length is about 0.3 nm) bringing strong columbic interactions to only those approached in vicinity of the wall surface. The absence of the gating effect at positive V_G for 100 nm-sized nanospheres (Fig. 2b) is hence attributed to less chance for the smaller particles to pass through the off-axial positions.). In contrast, the gating effects become weaker at lower $|V_G|$ causing little influence against the cross-membrane electric-field-dominated single-nanoparticle kinetics (Fig. 3c).

Electrical trapping of single-nanoparticles via gating control. Direct comparisons of the resistive pulses show marked difference in the motion degrees of freedom of the trapped nanoparticles. The I_{ion} curves reveal similar retention time of the particles irrespective of the gate polarity (Fig. 4a) but much larger fluctuations under negative V_G (Fig. 4b), which signifies more pronounced up-down movements of the nanobeads. Indeed, unlike the strong columbic attraction that immobilizes the nanoparticles on the wall surface, the counteracting hydrodynamic drag and electrophoretic forces are anticipated to induce stochastic motions in analogous to the objects trapped by gradient forces in laser focus[38,39]. These features were also observed in the
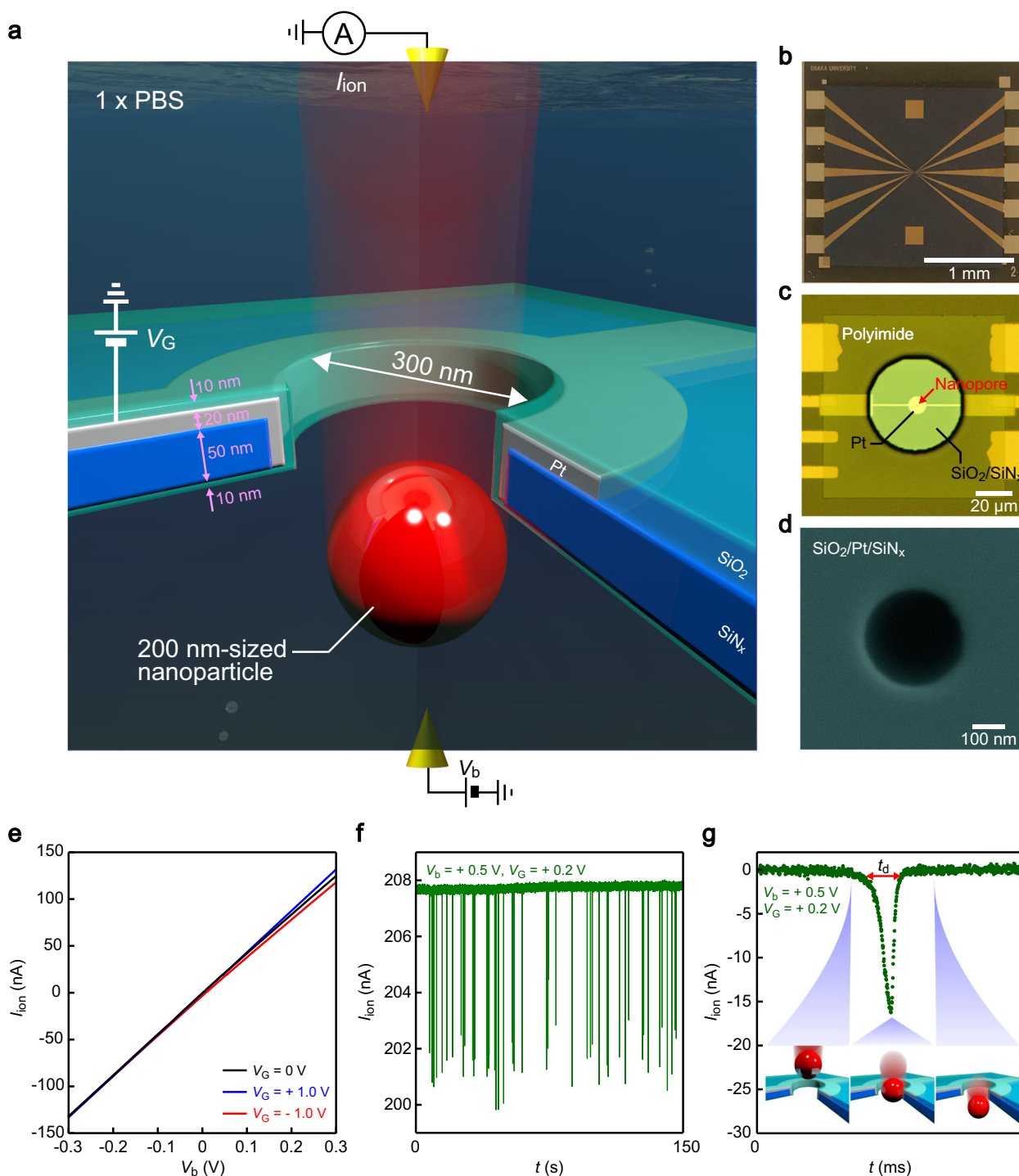
Fig. 1 Single-nanoparticle detections using a surround gate nanopore. a A schematic model depicting electrophoretic translocation of a 200 nm-sized carboxylated polystyrene nanobead through a 300 nm diameter surround-gate nanopore under the applied cross-membrane V_b and gate voltage V_G. Optical images of the nanopore chip showing an overview (**b**) and a magnified view at the center (**c**). The gate voltage was added to the Pt surround gate via the microelectrodes. Entire surface except the 50 μm region around the nanopore was coated with a thick polyimide layer for lowering capacitance-induced high-frequency noise of the cross-membrane ionic current I_{ion}. **d** A scanning electron micrograph of the 300 nm-sized gating nanopore. **e** I_{ion} versus V_b characteristics in 1× PBS under different V_G conditions. A partial I_{ion} versus time (t) trace (**f**) and a close view of a resistive pulse (**g**) occurred upon a nanoparticle passed through the nanopore. The width of the signal t_d represents the time required for the particle to move through the channel. The base current is offset to zero.

corresponding noise spectra (Fig. 4c) as stronger $1/f$ character-istics at $V_G = -1.05$ V attributed to the more prominent sto-chastic motions of the trapped particles.

We further investigated the vibration behavior by deriving the time-course change in the particle position z from the I_{ion} signals.

We conducted a three-dimensional finite element analysis of the ionic current blockade where we numerically estimated the cross-membrane ionic current through the gating nanopore with a rigid sphere of 200 nm diameter positioned at z along the pore axis (Fig. 5a)[40]. The obtained z versus I_{ion} pulse was then normalized
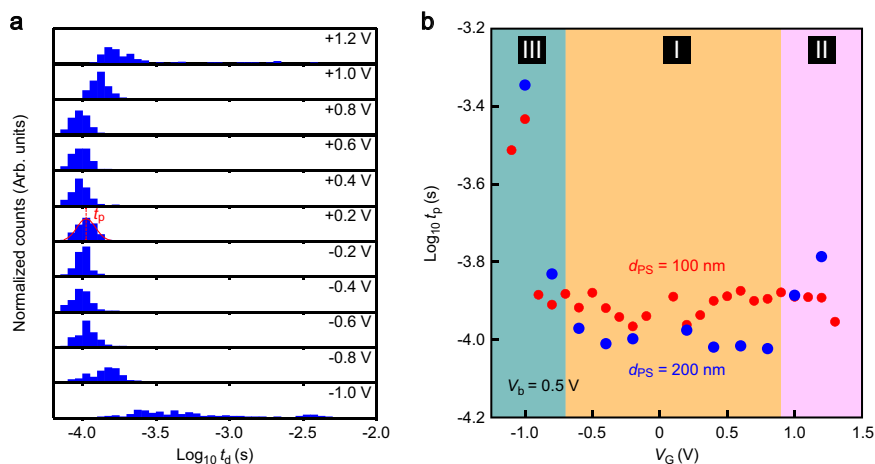
Fig. 2 Gate voltage dependence of the translocation time of single nanoparticles. a Histograms of t_d at different V_G conditions from -1.0 to $+1.2$ V under $V_b = 0.5$ V. Red curve displays Gaussian fitting that defines t_p at the peak position. **b** $\mathrm{Log}_{10} t_p$ versus V_G plots for the 200 nm- (blue) and 100-nm-sized nanobeads.
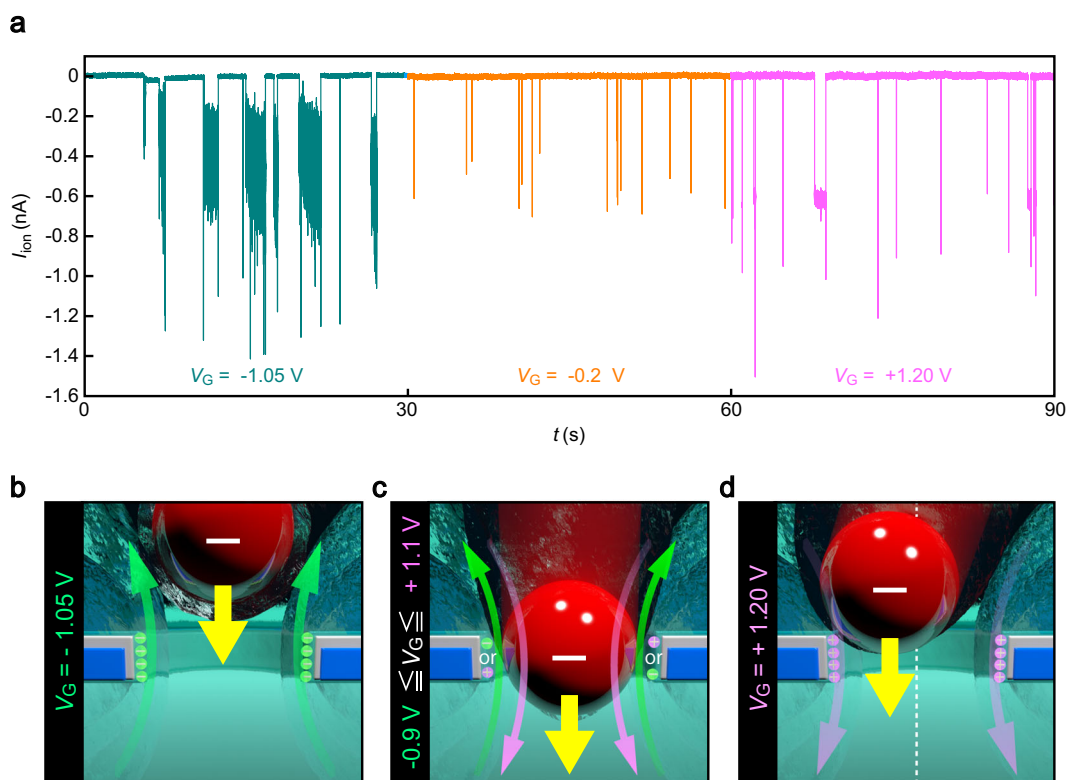

Fig. 3 Gate-dependent modes of single-nanoparticle dynamics. a Typical I_{ion} traces observed for 200 nm-sized nanoparticles in the three different V_G regimes under $V_b = 0.5$ V (orange: $V_G = -0.20$ V (I); pink: $V_G = +1.20$ V (II); cyan: $V_G = -1.05$ V(III)). The open pore current is offset to zero. Schematic explanations of the underlying mechanism. Green and pink balls describe, respectively, negative and positive electrical potentials induced at the SiO_2 wall surface by the gating. Under large negative V_G, the strong electroosmotic flow in direction opposite to the electrophoresis of the negatively-charged nanoparticles retard the translocation speed (**b**). When V_G is small, the electroosmotic flow becomes too weak to cause any notable influence on the electrophoretically-driven fast translocation motions of the particles irrespective of the voltage polarity (**c**). In case of large positive gate voltage conditions, the strong columbic interaction tends to temporarily trap the nanobeads when they come across the nanopore wall surface.

by the height (I_{norm}) and utilized as a reference to convert the experimental resistive pulses (Fig. 5b) into z versus t traces. For instance, the motion track elucidated the nanoparticles being adsorbed at 130 nm above the pore center under $V_G = +1.20$ V (Fig. 5c inset). In addition, the subsequent drop in the ionic current at around $t = 0.38$ s (Fig. 5b inset) suggested electrophoretic transits of the particles after desorption.

Vibration modes of electrically trapped nanoparticles. This single-nanoparticle tracking also led us to visualize the fluctuations under $V_G = -1.05$ V that took place at 187 nm and 166 nm above the channel with the amplitudes of 42 nm and 90 nm for the 200 nm- and 100 nm-sized particles, respectively (Fig. 5d–f). The underlying mechanism can be understood as oscillation of the spherical objects under the counteracting electrophoretic force
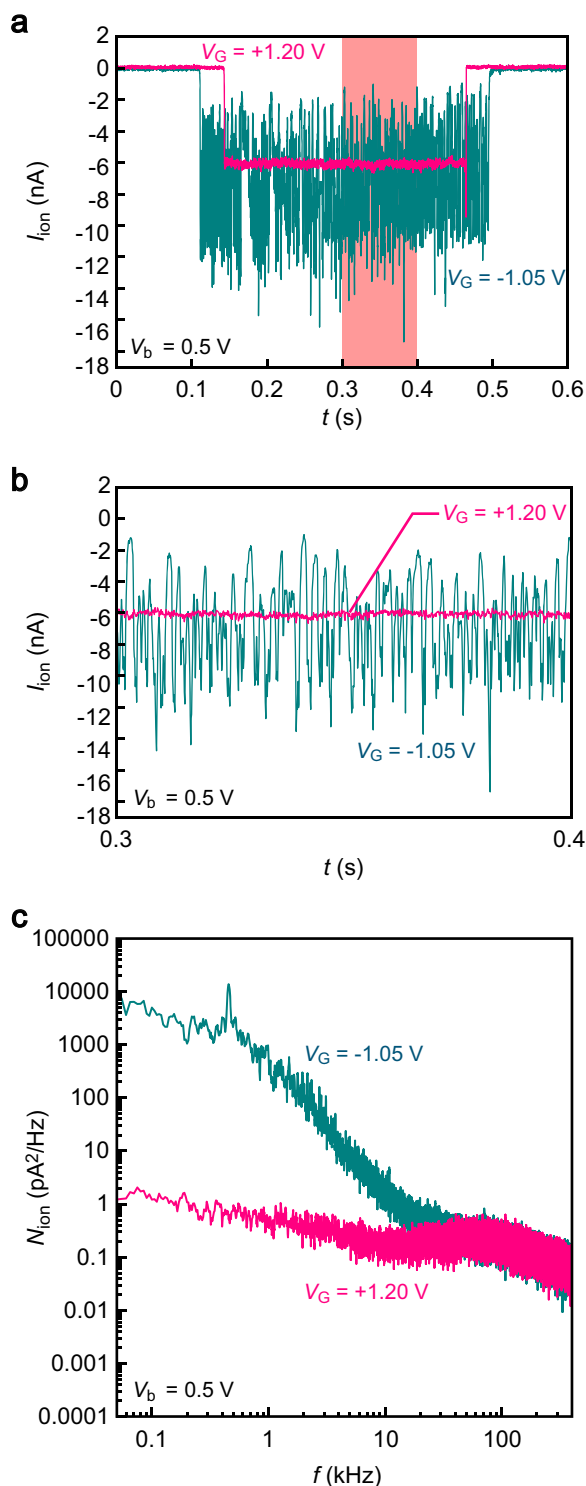
Fig. 4 Harmonic oscillation of single-nanoparticles. a Offseted I_{ion} curves presenting ionic current blockade by a 200 nm-sized nanoparticle under $V_G = -1.05$ V (cyan) and +1.20 V (pink). **b** Close-up views of the two signals in **a**. **c** Noise spectra of the $I_{ion} - t$ traces. Color code is the same as that in **a**.

F_{EP} and hydrodynamic drag force F_{EOF} by the electroosmosis-induced fluid flow coming out of the gating nanopore. To shed further light on the physical picture, we extended the numerical simulations to estimate the spatial distributions of the two forces acting on the nanoparticle (Supplementary Figs. S6–S8).

Specifically, the amount of surface charge q on the nanoparticles was assessed from the zeta potentials of −31 and −36 mV measured by a zeta sizer for the 200 nm- and 100 nm-sized particles, respectively, through Graham's equation[41,42]. The particle-position-dependent F_{EP} was then obtained as $-qE(z)$ where $E(z)$ is the electric field profile along the pore axis deduced by numerically solving Poisson, Nernst-Plank, and Navier–Stokes equations[43,44]. At the same time, the electroosmotically-driven fluid velocity $U(z)$ under the negative V_G was utilized to calculate the Stokes drag force F_{EOF} as $3\pi\eta d_{PS}U$. As a result, we found a crossover point at around $z = 200$ nm where F_{EP} becomes weaker than F_{EOF} as the 200 nm-sized nanobead moves toward the nanopore (Figs. 5g and 5h). The nanobeads were thus anticipated to be trapped at the position where F_{EP} balanced with F_{EOF}.

Here we remind that whereas the nanobead is anticipated to undergo harmonic oscillation under the electrophoretic and hydrodynamic drag forces at the orifice, the motion is in fact efficiently damped via viscous drag letting it to rest at the equilibrium point, which is akin to the principle of optical tweezer capable of trapping a transparent microscale object in a laser focal point via the gradient force emerging by the interplay between the induced dipole and the local electromagnetic field profile[45]. For example, the electrokinetics can be roughly described as a nanosphere of mass m vibrating in water with a spring constant k. This anticipates the particle to oscillate at a natural frequency f given as,

$$f = \frac{1}{2\pi}\sqrt{\frac{k}{m} - \left(\frac{3\pi\eta d_{ps}}{2m}\right)^2} \qquad (1)$$

Meanwhile, with the deduced k of 1.66 pN nm^{-1} from F_{EP} and F_{EOF} (Supplementary Fig. S9a, b), we find that $k/m < (3\pi\eta d_{ps}/2\,m)^2$, thus predicting overdamping of the harmonic oscillation. More directly, we also simulated the vibration motion by solving a Langevin equation with the Euler-Maruyama approach (Supplementary Fig. S9c-d). The results displayed random fluctuations of the particle positions by time instead of harmonic oscillations at a well−defined frequency, thereby corroborated negligible contributions of inertia due to the prominent influence of viscous drag. This in turn elucidated that the I_{ion} fluctuations at $V_G = -1.05$ V were of Brownian motions of the trapped nanobeads.

Ultrafine manipulation of single-nanoparticle translocation speed. The field-effect nanopore can be implemented not only for trapping particles but also to let them slowly move toward one direction. Even small deviations of V_G from −1.05 V were confirmed to induce unbalanced forces (Fig. 6a): $V_G \geq -0.9$ V offered inadequate hydrodynamic dragging to stop the electrophoretically-captured nanobeads (Supplementary Fig. S10) while $V_G \leq -1.1$ V yielded too strong electroosmotic flow that completely blocked the nanoparticles at the orifice (see also Supplementary Fig. S11 for the gating effect on 100 nm-sized nanoparticles demonstrating the trapping at –0.9 V). Yet, a subtle increase in the gate voltage from −1.05 V still allowed the nanoparticles to be hold in the trap zone with the center of mass now moving toward the pore under the slightly weaker water flow. The actual single-nanoparticle velocity v_{PS} was estimated by linear fitting to the z–t curve to be −59 nm s^{-1} at $V_G = -1.00$ V (Fig. 6b), which could be fastened by 17% to −69 nm s^{-1} through further decreasing the gate voltage to −0.96 V (Fig. 6c, d, see also Supplementary Fig. S12). The extremely low range of v_{PS} marks more than four orders of magnitude reduction in the single-particle velocity under no gate-control. This manifests the fact that while the gating control of electroosmotic flow[36] and particle trapping by hydrodynamic drag and electrophoretic forces[35] were separately reported previously, the combination of these
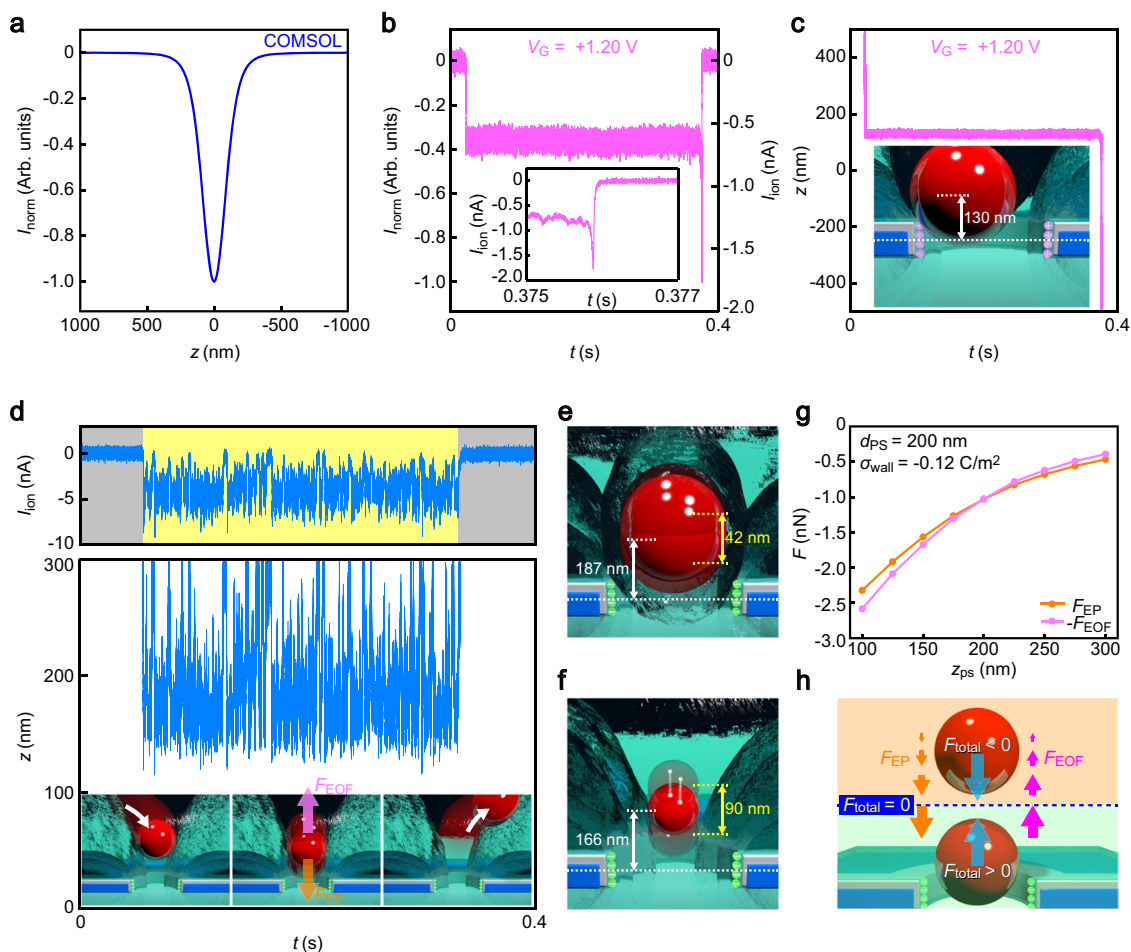
Fig. 5 Vibration modes of single-nanoparticles trapped by a field-effect nanopore. a Finite element analysis of ionic current blockade in the 300 nm-sized surround-gate nanopore by a 200 nm-sized nanoparticle under $V_b = 0.5$ V. z denotes the position of the center-of-mass of the spherical particle with respect to the middle of the nanopore. Open pore current is offset to zero. I_{norm} is the normalized ionic current by the height of the pulse. **b** A typical I_{ion} signal at $V_G = -1.20$ V. The inset shows a close view at the end of the signal wherein a sharp drop in the ionic current represents fast translocation of the surface-adsorbed nanoparticle after desorption. **c** Motion track of the nanoparticle in **b**. Inset image illustrates the location of the nanobead adsorbed on the positively-biased nanopore wall surface via the coulomb interactions. **d** A I_{ion} signal at $V_G = -1.05$ V and corresponding particle motions. The absence of the sharp edge at the end of the signal indicates repelling of the nanoparticle instead of electrophoretic translocation as depicted in the insets. Illustrative models depicting the motions of the 200 nm- (**e**) and 100-nm-sized nanoparticles (**f**) trapped at the surround-gate nanopore orifice under $V_G = -1.05$ V.
g The electrophoretic (F_{EP}) and the electroosmotic drag forces (F_{EOF}) on the nanoparticle positioned at z_{ps}. σ_{wall} is the surface charge density at the pore wall. The sign of F_{EOF} is inverted for the sake of clarity. **h** A schematic illustration describing the force balance at the nanopore orifice.

effects enables the ultra-fine control of single-nanoparticle translocation dynamics.

Discussion

It is worth discussing whether interference between the gate and the cross-membrane voltage can be a cause of the nanoparticle oscillation in the nanopore. Indeed, numerical studies predicted significant modulation of the electrostatic potential profile[31,32] that may create energy minima to trap a charged object inside the pore. To verify this point, we exhibited a control experiment using a SiN$_x$ nanopore without any gate electrode (Supplementary Fig. S13). It in fact revealed emergence of the corrugated resistive pulses suggestive of the particle traps inside the conduit under a specific V_b and pH conditions, the finding of which unambiguously prove the predominant role of electroosmosis on the trapping of nanoparticles demonstrated in the surround-gate nanopores.

As for the manipulation capability, the field-effect nanopore approach can be potentially used to accomplish 0.2 nt ms^{-1}, which

is the speed achievable only in biological nanochannels[15,18,19], when tentatively comparing with the translocation speed of single molecule DNA that generally passes through a solid-state nanopore at a rate faster than 100 nucleotides per ms (100 nt ms^{-1}). While it may require tagging of DNA on a nanocarrier surface for implementing genome sequencing[46], due to the soft nature of polynucleotides undergoing deformations by the counter-acting forces[47], the technique has an advantage over optical tweezers in sense that the mechanism involves no additional structure thus allowing compact device for mass production. Besides, it promises direct applications for resistive pulse analyses of small molecules such as proteins[10] and micro-RNA[48] where it is generally a prerequisite to slow-down their translocation dynamics for reliably detecting the associated ionic current blockade[8,17].

Methods

Fabrication of gating nanopores. A 4-in. 525 µm-thick Si wafer both sides coated with low-pressure chemical vapor deposition-grown 50 nm-thick SiN$_x$ layers was diced into 30 mm square chips. On the chip, Au microelectrodes were formed by photolithography followed by radio-frequency magnetron sputtering of Au
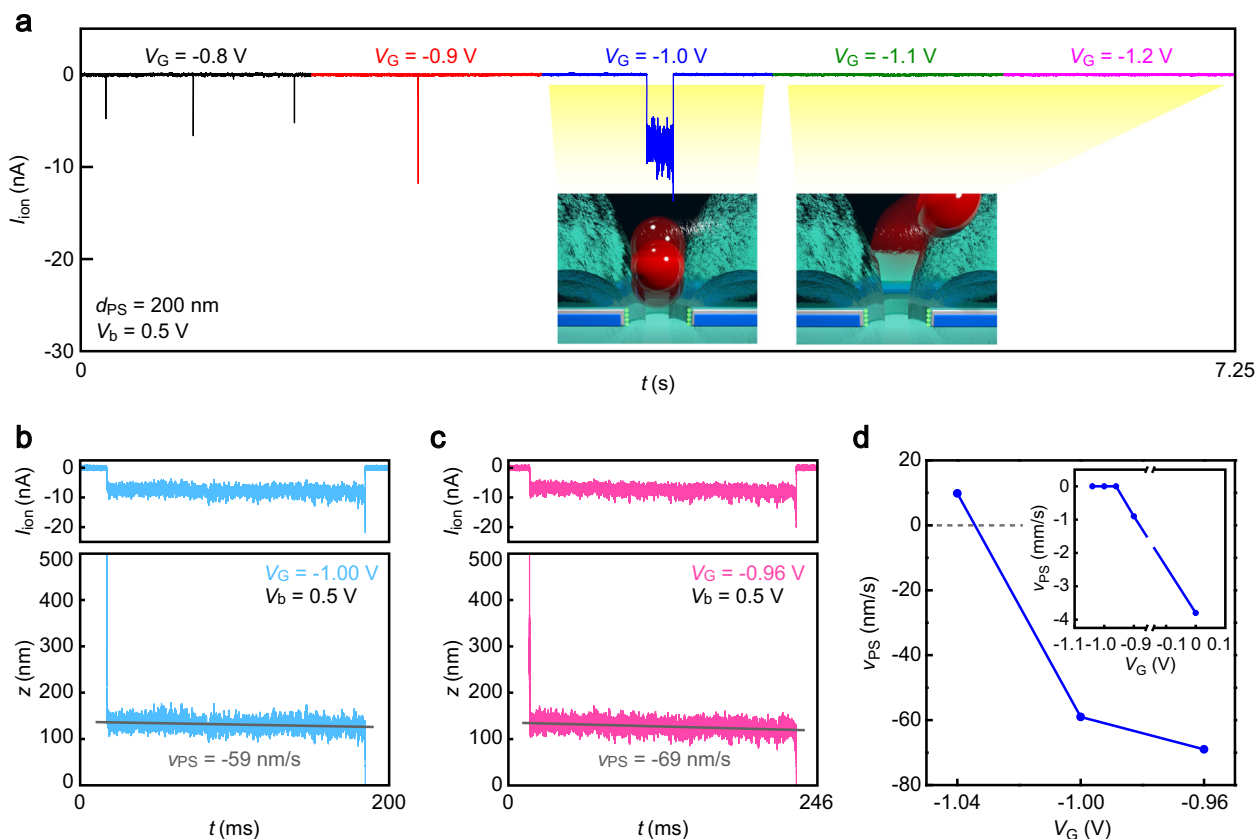
Fig. 6 Gate-controlled single-nanoparticle motions. a The effective range of V_G for the particle trap. The ionic current signals (top) and the corresponding z–t characteristics for 200 nm-sized nanoparticles captured under $V_G = -1.00$ V (**b**) and $V_G = -0.96$ V (**c**). Gray lines are linear fits to the curves whose slope signify the average velocity v_{ps} of the nanoparticles. **d** V_G-dependence of v_{PS}.

(20 nm)/Cr (5 nm) and lift-off in N,N-dimethylformamide (DMF, Wako) under ultrasonication. After that, the SiN$_x$ layer at the other side was partially removed by reactive ion etching with CF$_4$ etchant gas. The thus exposed Si layer was immersed in KOH aq. and heated to 80 °C for wet etching. As a result of the anisotropic nature of the etching process of the single-crystal Si led to a formation of a deep trench with ~50 nm-thick SiN$_x$ membrane at the bottom. Here, the membrane was arranged to be formed in the gap space between the Au microeletrodes by using the pre-designed external markers on the wafer surface. Subsequently, a gate electrode was fabricated by first delineating the pattern by an electron beam lithography using a resist ZEP-520A (Zeon). After development, Pt (20 nm) was deposited by the sputtering. The substrate was then put in DMF overnight for lift-off without sonication.

Integration of a polyimide micropore. The surround gate nanopore chip was covered by a photo-sensitive 5 μm-thick polyimide layer (Toray) by spin-coating and pre-baking. Then, the polyimide 50 μm around the nanopore was removed by photolithography. By the low-k polymer coating, we can ensure high temporal response of the ionic current as well as low noise platform by the reduced cross-plane net capacitance, which is a pre-requisite for reliable analyses of fast trans-location motions of nanoparticles by the resistive pulse measurements. Meanwhile, the thus formed polymeric micropore causes negligible influence on the cross-membrane ionic current due to the more two orders of magnitude larger size compared to the surround gate nanopore. Finally, the top surface including the exposed Pt electrode was coated with 10 nm-thick SiO$_2$ at the top and bottom sides by chemical vapor deposition. Here, the SiO$_2$ layer served as gate dielectrics as well as active surface to bond polydimethylsiloxane (PDMS) blocks for device sealing as explained in the following section.

Nanopore sealing. The polyimide-coated surround gate nanopore chip was sealed from the both sides by two PDMS blocks. The polymer blocks were obtained by first curing PDMS on a SU-8 mold on a Si wafer. The mold was fabricated in advance by spin coating SU-8 3000 (MICROCHEM), pre-baking, and photo-lithography. The SU-8 pattern had "I" shape so that after hardening the cured PDMS at 100 °C in oven, each block cut-out from the mold has I-shaped trench at one side of the surfaces. This trench served as a fluidic channel for letting nano-particle dispersion solution into the nanopore after the PDMS blocks were adhered

at both sides of the nanopore chip, which was exhibited by contacting the both surfaces after an oxygen plasma treatment.

Ionic current measurements. Electrolyte buffer 1 × PBS (Wako) was added from one side of the nanopore through inlet and outlet holes punched in the PDMS blocks in advance via the PDMS channel. At the other side, the same buffer containing 200 nm- or 100 nm-sized carboxylated nanobeads (Polysciences) was injected. Then, Ag/AgCl rods were inserted into the remaining holes in the PDMS blocks at the both sides. Using these as electrodes, the cross-membrane ionic current I_{ion} was recorded under the dc voltage V_b applied. Meanwhile, metal pins were contacted to the microelectrode pads to add the gate voltage. For the I_{ion}–V_b characteristics measurements, pico-ammeters Keithley6487 (Keithley) were used for adding voltage as well as to measure the ionic current. On the other hand, battery-based potentiostats were utilized for the resistive pulse measurements for the sake of better noise performance as voltage sources. Also, the current sampling was implemented at 1 MHz speed by using a home-built amplifier[40] backed by a fast digitizer (NI-5922, National Instruments) under a LabVIEW program control.

Data analytics. In order to extract resistive pulses from I_{ion} traces, the moving open pore current was first offseted to zero by subtracting the linearly-fitted base current in each of the 0.5 s sections. The positions of the pulses were then searched by finding local minima in the offseted curve using a threshold level set at -1 nA. Subsequently, resistive pulse signals were extracted by saving the data 0.01 s before and after the pulse apexes.

Finite element analysis. The ionic current flowing through the 300 nm-sized surround gate electrode embedded nanopore was simulated by a finite element method using COMSOL multiphysics 5.4 with AC/DC, Chemical Reaction Engineering, and Computational Fluid Dynamics modules. The nanopore structure was modeled as a cylinder of 8 μm-radius and 16.05 μm-height wherein a 50 nm-thick Si$_3$N$_4$ membrane (electrical conductivity of $\sigma = 1.4 \times 10^{-14}$ S m^{-1} and relative permittivity of $\varepsilon_r = 9.7$) covered with 30 nm-thick Pt and 20 nm-thick SiO$_2$ layers was placed at the middle. In the membrane, a through-hole with a radius of 150 nm was opened at the center. The nanopore as well as the cylinder was filled with water containing Na$^+$ and Cl$^-$ at a concentration of 137 mM with the mobility of,

respectively, 5.2×10^{-8} $m^2\,V^{-1}\,s^{-1}$ and 7.4×10^{-8} $m^2\,V^{-1}\,s^{-1}$. The ionic current was calculated by simultaneously solving Poisson equation, continuity equation at steady-state current, Nernst-Planck equation, and Naiver–Stokes equation under the potential difference of 0.5 V set between the top and bottom surface of the micrometer-scale cylinder and the wall surface potential to V_G.

The electrophoretic (F_{EP}) and electroosmotic drag force (F_{EOF}) were then estimated based on the obtained distributions of electric-field $E(r)$ and fluid velocity $u(r)$ as follows:

$$\overrightarrow{F}_{EP} = -e\oiint \overrightarrow{E}\sigma ds \qquad (2)$$

In the above, E is the electric field calculated from the above electrokinetic model, σ is the density of the negative charges on the nanoparticle surface with zeta potential of –31 mV as measured using a zeta sizer, and the integration was over the nanoparticle surface $\oiint ds$. On the other side, F_{EOF} was estimated through an integration of the viscous force density f_{EOF} on the nanoparticle surface:

$$\overrightarrow{F}_{EOF} = \oiint \overrightarrow{f}_{EOF} ds = -\eta \oiint \frac{\partial \overrightarrow{u}}{\partial r} ds \qquad (3)$$

where η is the viscosity of the solution and the partial differential $\partial u/\partial r$ represents the fluid velocity gradient along the nanoparticle-centered radial direction around the particle surface. Here we remind that a simplified estimation of F_{EOF} was provided through the Stokes equation $F_{EOF} = 3\pi d_{np}u$ where d_{np} is the diameter of the spherically-shaped nanoparticle and u is the average fluid velocity around the nanoparticle.

Data availability
The datasets generated during and/or analyzed during the current study are available from the corresponding authors on reasonable request.

References
1. Howorka, S. & Siwy, Z. Nanopore analytics: sensing of single molecules. *Chem. Soc. Rev.* **38**, 2360–2384 (2009).
2. Luo, L. et al. Resistive pulse analysis of nanoparticles. *Annu. Rev. Anal. Chem.* **7**, 513–535 (2014).
3. Shi, W., Friedman, A. K. & Baker, L. A. Nanopore sensing. *Anal. Chem.* **89**, 157–188 (2017).
4. McMullen, A., de Haan, H. W., Tang, J. X. & Stein, D. Stiff filamentous virus translocations through solid-state nanopores. *Nat. Comm.* **5**, 4171 (2014).
5. Arima, A. et al. Identifying single viruses using biorecognition solid-state nanopores. *J. Am. Chem. Soc.* **140**, 16834–16841 (2018).
6. Nawaz, M. et al. The emerging role of extracellular vesicles as biomarkers for urogenital cancers. *Nat. Rev. Urol.* **11**, 688–701 (2014).
7. Coumans, F. A. W. et al. Reproducible extracellular vesicle size and concentration determination with tunable resistive pulse sensing. *J. Extracel. Ves.* **140**, 16834–16841 (2018).
8. Plesa, C. et al. Fast translocation of proteins through solid state nanopores. *Nano Lett.* **13**, 658–663 (2013).
9. Si, W. & Aksimentiev, A. Nanopore sensing of protein folding. *ACS Nano* **11**, 7091–7100 (2017).
10. Varongchayakul, N., Song, J., Meller, A. & Grinstaff, M. W. Single-molecule protein sensing in a nanopore: a tutorial. *Chem. Soc. Rev.* **47**, 8512–8524 (2018).
11. Branton, D. et al. The potential and challenges of nanopore sequencing. *Nat. Biotechnol.* **26**, 1146–1153 (2008).
12. Heerema, S. J. & Dekker, C. Graphene nanodevices for DNA sequencing. *Nat. Nanotechnol.* **11**, 127–136 (2016).
13. Feng, J. et al. Identification of single nucleotides in MoS_2 nanopores. *Nat. Nanotechnol.* **10**, 1070–1076 (2015).
14. Coulter, W. H. Means of counting particles suspended in a fluid. US Patent No. 2656508 (1953).
15. Venkatesan, B. M. & Bashir, R. Nanopore sensors for nucleic acid analysis. *Nat. Nanotechnol.* **6**, 615–624 (2011).
16. Keyser, U. F. Controlling molecular transport through nanopores. *J. Roy. Soc. Interf.* **8**, 1369–1378 (2011).
17. Acharya, S. et al. Improved measurement of proteins using a solid state nanopore coupled with a hydrogel. *ACS Sens.* **5**, 370–376 (2020).
18. Cherf, G. M. et al. Automated forward and reverse ratcheting of DNA in a nanopore at 5-Å precision. *Nat. Biotechnol.* **30**, 344–348 (2012).
19. Nivala, J., Marks, D. B. & Akeson, M. Unfoldase-mediated protein translocation through an α-hemolysin nanopore. *Nat. Biotechnol.* **31**, 247–250 (2013).
20. Fiori, N. D. et al. Optoelectronic control of surface charge and translocation dynamics in solid-state nanopores. *Nat. Nanotechnol.* **8**, 946–951 (2013).
21. Chou, C.-F. et al. Electrodeless dielectrophoresis of single- and double-stranded DNA. *Biophys. J.* **83**, 2170–2179 (2002).
22. Tanaka, S. et al. Tailoring particle translocation via dielectrophoresis in pore channels. *Sci. Rep.* **6**, 31670 (2016).
23. Luan, B. et al. Base-by-base ratcheting of single stranded DNA through a solid-state nanopore. *Phys. Rev. Lett.* **104**, 238103 (2010).
24. Nam, S.-W., Rooks, M. J., Kim, K.-B. & Rossnagel, S. M. Ionic field effect transistors with sub-10 nm multiple nanopores. *Nano Lett.* **9**, 2044–2048 (2009).
25. Ren, R. et al. Nanopore extended field-effect transistor for selective single-molecule biosensing. *Nat. Comm.* **8**, 586 (2017).
26. Tsutsui, M. et al. Temporal response of ionic current blockade in solid-state nanopores. *ACS Appl. Mater. Interf.* **10**, 34751 (2018). 34757.
27. Rosenstein, J. K., Wanunu, M., Merchant, C. A., Drndic, M. & Shepard, K. L. Integrated nanopore sensing platform with sub-microsecond temporal resolution. *Nat. Methods* **9**, 487–492 (2012).
28. Tabard-Cossa, V., Trivedi, D., Wiggin, M., Jetha, N. N. & Marziali, A. Noise analysis and reduction in solid-state nanopores. *Nanotechnology* **18**, 305505 (2007).
29. Garaj, S. et al. Graphene as a subnanometre trans-electrode membrane. *Nature* **467**, 190–193 (2010).
30. Tsutsui, M. et al. Single-nanoparticle detection using a low-aspect-ratio pore. *ACS Nano* **6**, 3499–3505 (2012).
31. Liu, Y., Huber, D. E., Tabard-Cossa, V. & Dutton, R. W. Descreening of field effect in electrically gated nanopores. *Appl. Phys. Lett.* **97**, 143109 (2010).
32. Liu, Y., Huber, D. E. & Dutton, R. W. Limiting and overlimiting conductance in field-effect gated nanopores. *Appl. Phys. Lett.* **96**, 253108 (2010).
33. He, Y. et al. translocation through gate modulation of nanopore wall surface charges. *ACS Nano* **5**, 5509–5518 (2011).
34. Yeh, L.-H., Xue, S., Joo, S. W., Qian, S. & Hsu, J.-P. Field effect control of surface charge property and electroosmotic flow in nanofluidics. *J. Phys. Chem. C* **116**, 4209–4216 (2012).
35. Stein, D. et al. Electronic concentration of DNA polymers in nanofluidic channels. *Nano Lett.* **10**, 766–772 (2010).
36. Schasfoort, R. B. M., Schlautmann, S., Hendrikse, J. & van den Berg, A. Field-effect flow control for microfabricated fluidic networks. *Science* **286**, 942–945 (1999).
37. Chen, P. et al. Atomic layer deposition to fine-tune the surface properties and diameters of fabricated nanopores. *Nano Lett.* **4**, 1333–1337 (2004).
38. Block, S. M. Making light work with optical tweezers. *Nature* **360**, 493–495 (1992).
39. Grigorenko, A. N., Roberts, N. W., Dickinson, M. R. & Zhang, Y. Nanometric optical tweezers based on nanostructured substrates. *Nat. Photon.* **2**, 365–370 (2008).
40. Tsutsui, M. et al. Particle trajectory-dependent ionic current blockade in low-aspect-ratio pores. *ACS Nano* **10**, 803–809 (2016).
41. O'Brien, R. W. & White, L. R. Electrophoretic mobility of a spherical colloidal particle. *J. Chem. Soc. Farad. Trans. 2*, 1607–1626 (1978).
42. Arjmandi, N., Roy, W. V., Lagae, L. & Borghs, G. Measuring the electric charge and zeta potential of nanometer-sized objects using pyramidal-shaped nanopores. *Anal. Chem.* **84**, 8490–8496 (2012).
43. Laohakunakorn, N., Thacker, V. V., Muthukumar, M. & Keyser, U. *Nano Lett.* **15**, 695–702 (2015).
44. German, S. R., Luo, L., Henry, H. S. & Mega, T. L. Controlling nanoparticle dynamics in conical nanopores. *J. Phys. Chem. C* **117**, 703–711 (2013).
45. Li, T., Kheifets, S., Medellin, D. & Raizen, M. G. Measurement of the instantaneous velocity of a Brownian particle. *Science* **328**, 1673–1675 (2010).
46. Keyser, U. F. et al. Direct force measurements on DNA in a solid-state nanopore. *Nat. Phys.* **2**, 473–477 (2006).
47. Aksimentiev, A. Deciphering ionic current signatures of DNA transport through a nanopore. *Nanoscale* **2**, 468–483 (2010).
48. Wanunu, M. et al. Rapid electronic detection of probe-specific microRNAs using thin nanopore sensors. *Nat. Nanotechnol.* **5**, 807–814 (2010).

Author contributions
M.T., T.W., K.T., and T.K. planned experiments. M.T. and S.R. fabricated Surround-gate nanopores and performed resistive pulse measurements of single-nanoparticles. K.Y. and Y.H. performed finite element analyses of ion transport and nanoparticle translocation dynamics in the nanopores. M.T. and T.K. co-wrote the manuscript.

Competing interests
The authors declare no competing interests.

Additional information

Supplementary information The online version contains supplementary material available at https://doi.org/10.1038/s43246-021-00132-3.

Correspondence and requests for materials should be addressed to M.T. or T.K.

Peer review information Primary handling editor: Aldo Isidori.

Reprints and permission information is available at http://www.nature.com/reprints

Publisher's note Springer Nature remains neutral with regard to jurisdictional claims in published maps and institutional affiliations.